DUAL TRACKED MOBILE ROBOT FOR MOTION IN CHALLENGING TERRAINS

Shraga Shoval
Department of Industrial Engineering and Management,
Ariel University Center, Ariel, Israel
shraga@ariel.ac.il

Amir Shapiro
Department of Mechanical Engineering,
Ben Gurion University of the Negev,
Beer-Sheva, Israel
ashapiro@bgu.ac.il

Abstract

In this paper we present a novel design for a dual tracked mobile robot. The robot is designed for safe, stable and reliable motion in challenging terrains, tunnels and confined spaces. It consists of two tracked platforms connected with a semi-passive mechanism. Sensors attached to the connecting mechanism provide redundant localization data that improves the vehicle's autonomous dead reckoning. Each tracked platform mechanically backs-up the other platform, resulting in a more robust and reliable operation. The load share between the platforms enables high payload to weight ratio even on soft and slippery terrains. The robot's configurations makes it suitable for motion in confined spaces such as underground tunnels, collapsed structures, pipes and caves. The paper presents the mechanical design of the robot, its kinematic model, stability analysis and a motion planner. Experimental results conducted on prototype models in various types of environments verify the robot capabilities to operate successfully on challenging terrains. The dual tracked robot is capable of climbing slopes 50% steeper than a single robot can. Moreover, the improved odometry system shows high accuracy with 2% error of the total travel distance.

I. Introduction

Unmanned Ground Vehicles (UGVs) are used for various off-road applications, including space explorations, security missions, agriculture, search and rescue, subterranean missions and many more. Off-road vehicles have been investigated for a long time, both for wheeled and tracked vehicles. While wheels are efficient for motion on relatively smooth and flat surfaces, tracked vehicles offer several advantages for motion on rough terrains. A U.S. Army survey (Hornback, 1998) shows that when on well-structured

surfaces, wheeled vehicles demonstrated excellent mobility and speed, but when off-road usage was required, and soft, wet or slippery conditions prevailed, tracked vehicles show better performance. Tracked vehicles provide significantly better travel times and stability when the mission requires off-road usage greater than 60 percent of the time or distance, and in some cases tracked configuration guarantees the best mobility for unrestricted, all weather tactical operations. From a mobility perspective, tracked vehicles offer the best solution for versatile mobile platforms that are required to operate over diverse terrain, because tracks inherently provide a greater surface area than wheels (Unger, 1998). However, autonomous unmanned tracked vehicles introduce some drawbacks that limit their use. It takes considerable power to steer a tracked vehicle, since the leading and trailing ends of the footprint, or contact patch, skid sideways, perpendicular to the direction the tracks roll (skid steering). The worst case is the neutral turn (when the vehicle performs pure rotation around its center), which may well require as much power to execute as to travel at full speed. In addition, skid steering results in unreliable odometry, and the position error is often as large as the total traveled distance. This makes autonomous positioning and motion control for tracked vehicles complex. In addition, tracked mechanisms tend to accumulate dirt, sand, and stones around the driving gears that may result in snapped or derailed tracks.

Some models for slip estimation have been developed (Yoshida and Hamano, 2002, Shiller and Serate, 1995), but they require adequate data on the surface traversed by the vehicle. This data may not be available or accurate enough when operating in unknown environments. Some systems improve the performance and autonomy of the UGV by acquiring information from the terrain, through identifying soil parameters using physical

models and numerical techniques. For example, Zweiri, et. al. (2004) and Tan et. al. (2003) use on-line identification systems to estimate friction coefficients in excavation missions.

A different approach to overcome some of the difficulties encountered in traversing rough terrain using tracked vehicles is to operate two or more vehicles in tandem. Advantages of operating in this manner include a wider effective wheel base to prevent the vehicle from overturning, and that the vehicles can help each other to overcome obstacles such as steep up or down slopes by employing a push-pull effect. Such an arrangement is described in Burrz et al (2003). Connecting the two platforms is performed by means of two coupling devices, one mounted at the center of the back end of the leading platform, and the second at the center of the front end of the trailing platform. The coupling device consists of a ball and socket mechanism, which allows a maximum angular motion between the two platforms, and permits vertical motion. The coupling device can be either passive or active. In the active mode, a gear motor that determines the relative orientation between the two platforms actuates the coupling device. However, the coupling between these two robots has several limitations:

— In either the passive or active mode there is no option for relative lateral motion between the two platforms, and the angular motion of one platform is constrained by the other platform, resulting in restricted maneuverability while engaged.

— No mechanism exists for relative configuration measurements between the two platforms; therefore the accuracy of the whole system is limited.

In this paper, we present the design of a dual tracked robot with a mechanical linkage between them. The design allows for improved mobility, accuracy and efficiency in autonomous and semi-autonomous robotic missions in unknown environments, particularly in confined spaces such as tunnels and pipes. Robotic mission in confined spaces like tunnels and pipes differs from surfaced robotic missions in several aspects:

-**Communication**: although robotic vehicles can operate autonomously for various periods, communication with the operator and other off-board agents (sensors, controllers etc.) is often essential for safe and reliable completion of the mission. Communication in confined spaces is limited due to limited or lack of wireless communication channels, and the mechanical complexity of wired communication.

-**Localization**: due to the limited or lack of wireless communication in confined spaces, autonomous robots must rely entirely on their on-board, self-localization capabilities (dead reckoning). Inertial and odometric localization methodologies, which are the major independent on-board localization techniques, have limited accuracy that is reduced over time and distance, and subjected to external disturbances such as slippage, uneven surfaces and skids.

-**Maneuverability**: defined as the ability of the robot to perform a controlled series of changes in movements toward an objective configuration, maneuverability can become complex or even unfeasible in confined spaces. Limitations on maneuverability can be due to the dimensions of the vehicle relative to the free space, and/or due to constraints over the vehicle capabilities to perform the required changes in motion.

- **Stability**: a safe and reliable motion of an autonomous vehicle requires continuous satisfaction of static and dynamic constraints. This is particularly important when the

vehicle travels over complex terrain with steep slopes, when the surface is slippery, or when inertial forces are large. A vehicle in a stable state can become unstable for several reasons:

1) Large inertial forces arising from rapid acceleration or deceleration, or tight turns.

2) Gravitational and reaction forces due to complex terrain geometries.

3) Surface conditions.

4) Unexpected external disturbances.

Unstable motion can result in slippage, loss of contact with the ground and possible tip over. This can cause **unrecovered** consequences as the limited access to the troubled vehicle due to the confined space may prevent assistance.

We present a robot designed to overcome the above-mentioned constraints, allowing a safe, reliable and stable motion even in extreme terrains such as underground narrow tunnels, soft or wet surfaces, steep slopes and confined spaces. The paper is organized as follows: Section II describes the mechanical design of the robot, Section III provides stability analysis, Section IV discusses the odometric model of the robot, Section V describes the control models and motion planning, Section VI describes the user interface and Section VII the experimental results conducted with the prototype robots.

II. Mechanical Design

The mechanical design is based on a modified spatial version of a four-linkage mechanism in which an upper beam is connected to two tracked driving units with two connecting bars, using six revolute joints. Figure 1 shows a schematic description of the system. As shown, the two tracked platforms (that can be extended to more platforms

connected to the others with similar mechanisms) are configured to travel in tandem, and a mechanical linkage connects the platforms to each other. The mechanical linkage enables efficient forces and moments transmission between the platforms and comprises two connecting bars, three revolute joints on each of the units, and an adjustable connecting beam that connects the connecting bar on one platform with the connecting bar on the other platform. The length of the connecting beam can be manually adjusted using two sliding cartridges and screws.

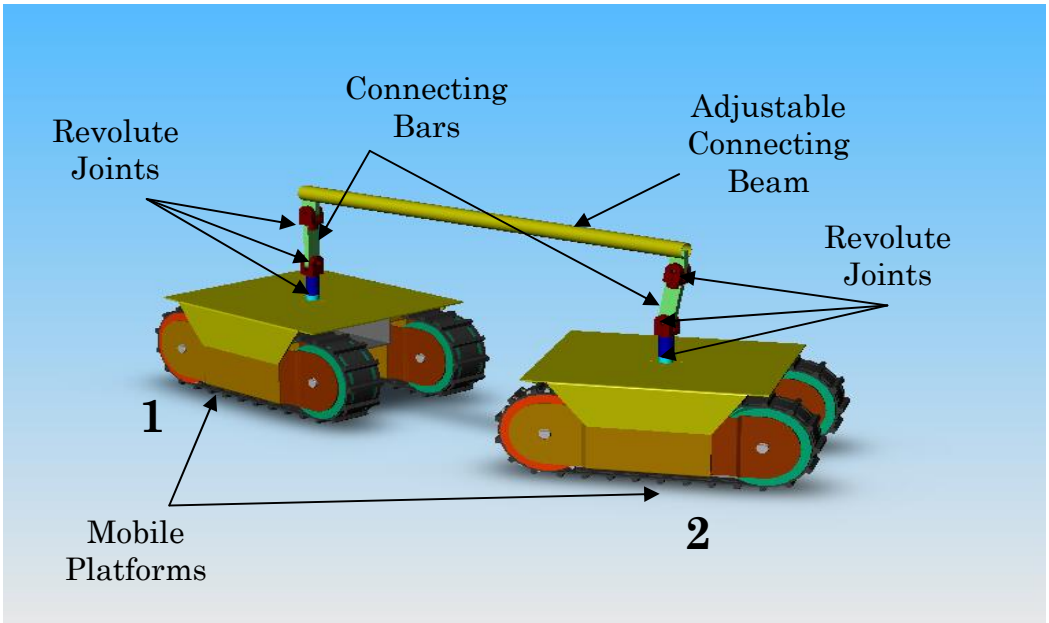

Figure 1: Schematic description of the robot, consisting of two tracked platforms, two connecting bars (on each platform), and one connecting beam. Six revolute joints join the connecting bars and beam to the platforms.

The six revolute joints allow independent relative motion between the two tracked driving units. These relative motions are measured, using potentiometers (or encoders) attached to each joint. Figure 2 shows the connecting mechanism and its six revolute joint.

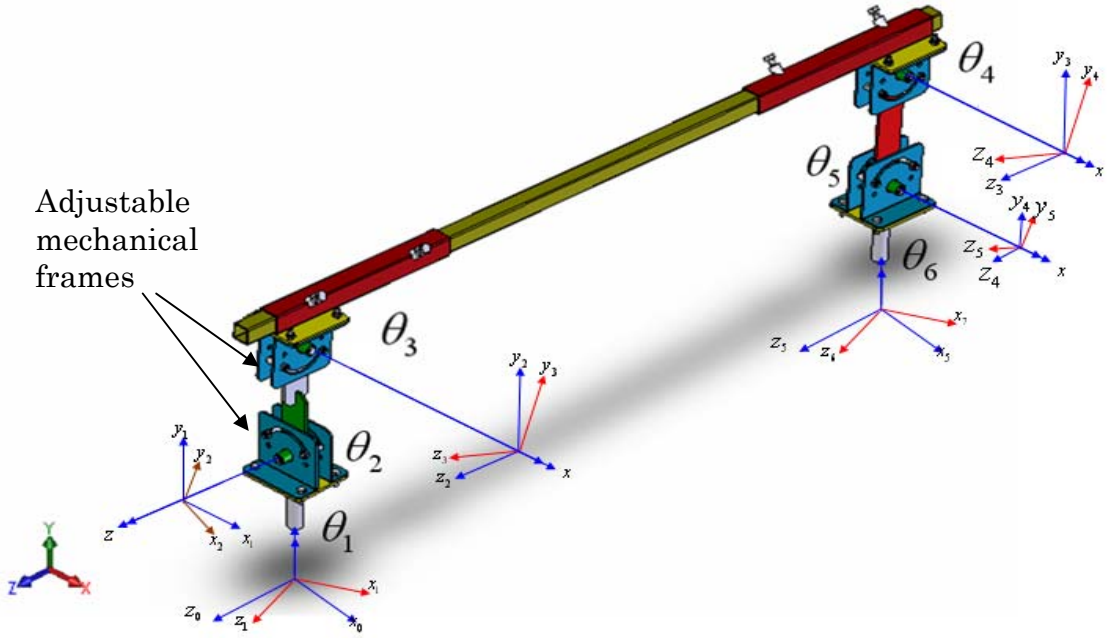

Figure 2: The connecting mechanism and its 6 revolute joints. Two joints (1 and 6) allow unlimited rotation of the platforms around the connecting bars, while the other four joints allow only limited motion. Notice the asymmetric configuration of the revolute joints on the connecting bars (joint 2 and joint 5).

One of the revolute joints on each unit connects the bottom of the connecting bar to the top of the tracked unit, allowing unlimited revolution of the connecting bar around an axis perpendicular to the upper surface of the unit (θ_1 and θ_6), while the other four revolute joints have limited motion, bounded by adjustable mechanical frames. Notice that the configuration of the joints is not symmetric: while the revolute axes of θ_4 and θ_5 are parallel in the lateral direction of the connecting beam, the revolute axis of θ_2 and θ_3 are perpendicular to each other. The revolute axis of θ_3 is in the lateral direction to the connecting beam, while θ_2 is in the longitudinal direction. This asymmetric configuration between the two units allows for independent six degrees of freedom motion of each unit.

As mentioned, the limited motions of θ_2, θ_3, θ_4 and θ_5 are bounded by the mechanical frame of each joint, and can be adjusted using two adjusting stoppers attached at each side of the joint. The joints with limited motion have two possible configurations: passive and active. In the passive configuration, the joint is within its motion limits, and is therefore free to move around its revolute axis. In the active configuration, the joint has reached the limit of its motion and further movement is only possible in the opposite direction. In this configuration, the joint can transfer forces and moments from one platform to the other. As mentioned, the mechanical stoppers on the joint frame adjust the range of mobility of the joint. Each tracked platform can move freely regardless of the motion of the other platform, as long as all six joints of the connecting mechanism are within the limits of their motion. However, when one or more joints reach their limits, the configuration of one platform limits the motion of the other platform. In this case, forces and moments are transferred between the platforms by the connecting mechanism. Figure 3 shows a few configurations where the joints reach their limits and transfer forces. In this figure, joint θ_3, θ_4 and θ_5 reach their limits, allowing longitudinal force transmission along the connecting beam. Figure 3(a) shows the configuration in which platform #1 pulls platform #2 to the left. Figure 3(b), shows a configuration in which platform #1 pushes platform #2 to the right.

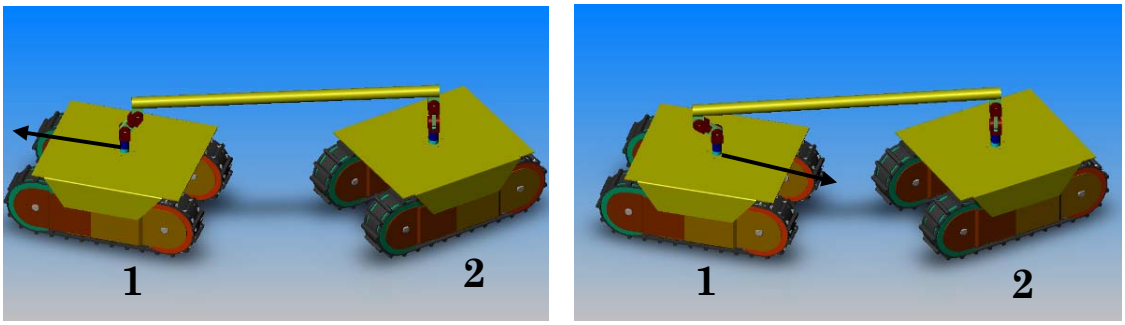

(a) (b)

Figure 3: Configurations in which platform #pushes (3(a)) or pulls (3(b)) the other platform. In both cases some joints reach their limit, allowing force transfer from platform #1 to platform #2.

Each platform contains its own power supply. This way, one platform can pull or push the other platform in case of a failure in one of them. As mentioned, this is crucial when operating in confined spaces, where external assistance cannot reach the troubled platform. Two-way communication with the robot can be wireless, or by means of a cable. When the communication is by means of a cable, a winch system is mounted on the rear platform for transporting, releasing, and rewinding the cable. The winch synchronizes the amount of cable released during forward motion, and rewinds it during reverse motion. The winch is required for motion in confined spaces where wireless communication is not allowed or possible, and pulling a cable is impractical due to the load of the cable and the friction that may develop when turning several times along the path.

III. Stability Analysis

Figure 4 shows a schematic 2D description of the robot traversing over a partially linear concaved terrain. When the two platforms are independently stable, they must be in a quasistatic equilibrium. In such a configuration, all the revolute joints are in their intermediate configuration and the platforms do not exchange forces and/or moments. However, when one of the platforms is not in a quasistatic equilibrium, it is subject to uncontrolled motion. As a result, the revolute joints on the connecting mechanism rotate until they reach their motion constraints, and forces and moments are transmitted through the connecting mechanism. If the platform, which is still in equilibrium state, can transfer enough forces and moments to keep the other platform in equilibrium, the entire system

is considered a stable rigid body in equilibrium. In our stability analysis, which examines the system just before becoming unstable, we consider the entire system a single rigid body in which the mass is concentrated between the two platforms. For simplicity, we assume that the masses of both platforms are significantly higher than the mass of the connecting mechanism, and as a result, the center of mass of the whole system is located at the center of the imaginary line connecting the centers of mass of the two platforms. Figure 4 shows three (out of many) possible configurations for traversing over the slope. In this figure, the center of mass of the entire system is shown as a sphere located on the line connecting the centers of mass of the two platforms (the dashed line).

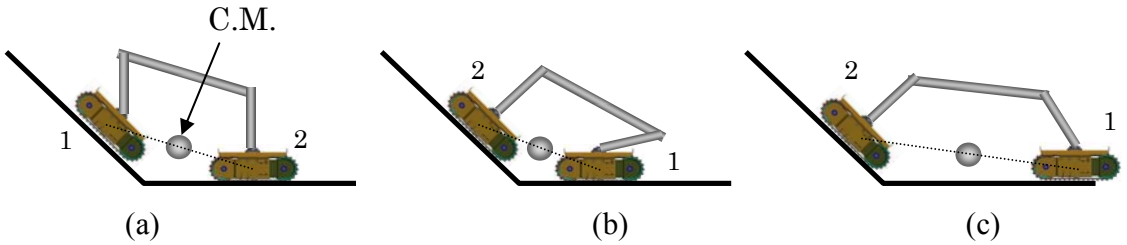

Figure 4: Different configurations for traversing over a slope. In 4(a) platform #1, while in 4(b) and 4(c) platform #2 leads. In 4(b) platform #1 pushed platform #1, while in 4(c) platform #2 pulls platform #1.

Combining the two platforms and the connecting mechanism to a single rigid body, and assuming a quasistatic motion in which inertial forces are negligible compared with all other forces, the vehicle is in equilibrium only if

$$\begin{aligned} \sum F_c + F_g + \sum F_e &= 0 \\ \sum F_c r_c + \sum F_e r_e + \sum M_e &= 0 \end{aligned} \qquad (1)$$

where F_c are the contact forces between the tracks and the ground, F_g is the gravitational force concentrated at the center of mass, F_e are additional external forces, M_e is additional external Moment, r_c and r_e are position vectors from contact and external forces to the center of mass.

Contact forces - F_c consist of normal forces - f^n pointing normal to the surface, and friction forces f^f tangent to the surface. Assuming Coulomb friction law, the friction force at contact *i* is bounded by $f_i^f \le \mu_i f_i^n$ (μ_i is the coefficient of friction between the track and the ground at contact *i*), therefore the total reaction force at contact *i* is bounded by the friction cone FC_i with a span $\theta_i = 2\tan^{-1}(\mu_i)$. If no external forces and torques are applied on the robot, and contacts with the ground are limited to two points (one point at the center of each platform), all reaction forces must intersect at the robot's center of mass in order to keep the entire system at equilibrium. Since the action lines of the reaction forces are bounded by the friction cone, stability requires that the location of the center of mass (though which the gravitational force acts vertically) is within the vertical strip spanned by the intersection of all friction cones (Or and Rimon, 2006). Another constraint is that normal forces at contacts must not be negative (unless a grasping mechanism is used). This constraint further reduces the permissible locations of the center of mass to a vertical strip bounded by the intersection of the two external contacts with vertical strip generated by the intersection of the two friction cones. Figure 5 illustrates these boundaries. The vertex of friction cone FC_1 is at contact 1, and the vertex of friction cone FC_2 is at contact 2. The vertical lines *A* and *C* are on contact points 1 and 2 respectively. Vertical line *B* is on the left boundary of the intersection between the two friction cones (FC_1 and FC_2) and line *D* is on the right boundary of the intersection. In this case, equilibrium is possible if the robot's center of mass is within the *Stable Vertical Strip (SVS)*, which is bounded by lines *B* and *C* (the hatched area). In the configuration shown in the figure, the center of mass is on line B, indicating that the system is on its equilibrium limit.

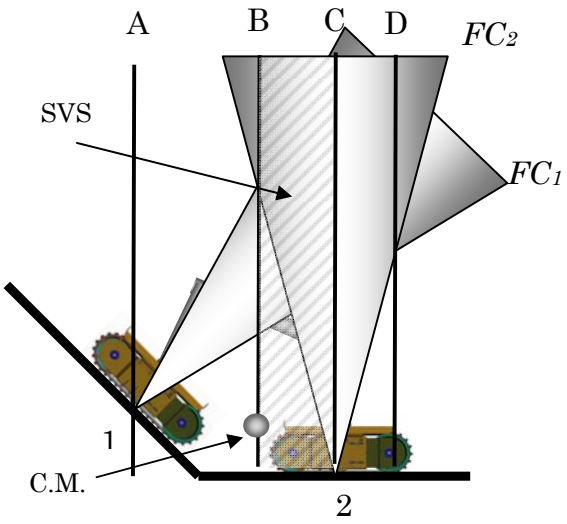

Figure 5: Friction cones and *Stable Vertical Strip* (SVS) for the dual tracked robot. The intersection of the two friction cones and the vertical lines through the contact points construct the *SVS* between vertical line *B* and vertical line *C*.

Or and Rimon's theory deals with mechanisms with a pre-defined number of contacts and locations. The number of contacts with the ground and their position relative to the center of mass for wheeled vehicles or other mobile mechanisms with distinct footpads is well defined. However, in tracked vehicles there are uncertainties about the number of contacts and their location along the track. Ideally, the weight of a tracked vehicle is evenly dispersed over the entire contact area of the track with the ground. However, surface geometry, ground texture, track tension and the suspension mechanism significantly affect the contacts between the tracks and the ground. There might be several contacts along each track, affecting the vehicle's response to driving commands, and reducing the accuracy of odometry. In addition, given that stability depends on the position of the center of mass relative to the contacts with the ground, it is more difficult with this type of mechanism to determine configurations that guarantee stability. The rest of this section discusses the necessary adjustments required for the stability analysis of tracked vehicles.

We first examine the scenario where contact forces are spread along the entire track with a known distribution. The magnitude (F_r) and location ($\bar{x}$) of the resultant force is given by

$$F_r = \int_{x=0}^{l} f_c dx$$
$$\bar{x} = \frac{\int_{x=0}^{l} f_c x dx}{\int_{x=0}^{l} f_c dx} \quad (2)$$

where f_c is the distributed contact force along the track, l is the length of the track in contact with the surface and $\bar{x}$ is the location of the resultant force on the track relative to one end.

In the general case, the resultant force is within a friction **trapezoid** FT_i rather than a friction cone, as shown in Figure 6. The *SVS* generated by the intersection of the two friction trapezoids, combined with the constraints of non-negative normal forces at contacts, is similar to the one shown in Figure 5. The vertical lines A and C are the external vertices of the trapezoid, and vertical lines B and D are on the intersection points of the two friction trapezoids. However, this *SVS* cannot guarantee stability since the location of the contact force along the tracks is unknown. Furthermore, if more than two contacts are applied simultaneously on the robot, the analysis described in the previous section is invalid.

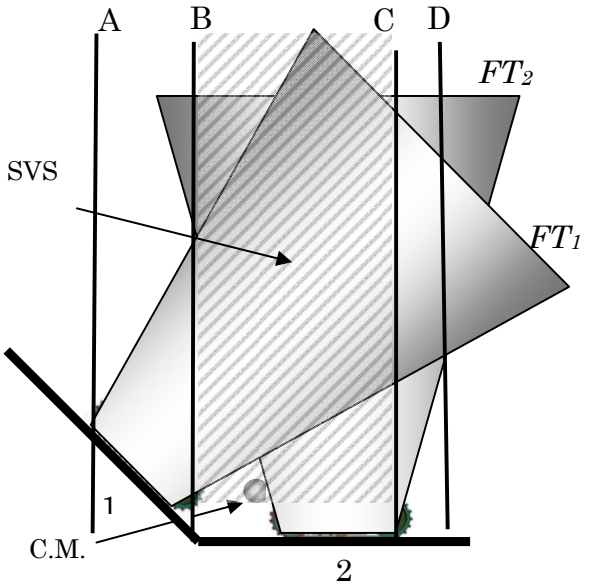

Figure 6: SVS for contact forces spread along the tracks. Instead of friction cones there are friction trapezoids. The SVS is constructed by the intersection of the friction trapezoids and their vertices.

As mentioned, the ideal assumption that contact forces spread evenly along the contact area between the track and the surface is often not realistic. Bumps and holes in the ground affect the magnitude, direction and exact location of the interaction forces. Bumps can create a concentrated reaction force applied at the highest spot of the bump in a normal direction to the bump. Holes, on the other hand, reduce the contact area between the track and the ground, changing the magnitude and location of the reaction forces. Figure 7 shows an example where one track (on the left) has a single contact at the center (point #1), while the second track (on the horizontal surface) has two possible contacts either at point #2 and/or at point #3 (the edges of the track). Figure 7a illustrates the three friction cones and all vertical lines (constructed either by the intersections of the friction cones or by the contact points). Lines A, D and F are on contacts 1, 2 and 3 respectively. Lines B and E are on the intersection between FC_1 and FC_2. Lines C and G are on the intersection between FC_1 and FC_3. Figure 7b shows the SVS_1 for contacts at points 1 and 2, generated by intersection of FC_1 and FC_2. SVS_1 is bounded on the left by line B (left

intersection of FC_1 and FC_2). On the right SVS_1 is bounded by line D which is the vertical line on contact 2. SVS_2, for contacts at points 1 and 3 is bounded on the left by line C (left intersection of FC_1 and FC_3) and on the right by line F which is the vertical line on contact 3. Any other combination of contacts between points 2 and 3 (while contact 1 maintains its original location) generates a new friction cone and a new *SVS*. However, the new *SVS* is bounded by the external boundaries of the two *SVS's* (FC_2 and FC_3) constructed by the two extreme contacts (lines B and F).

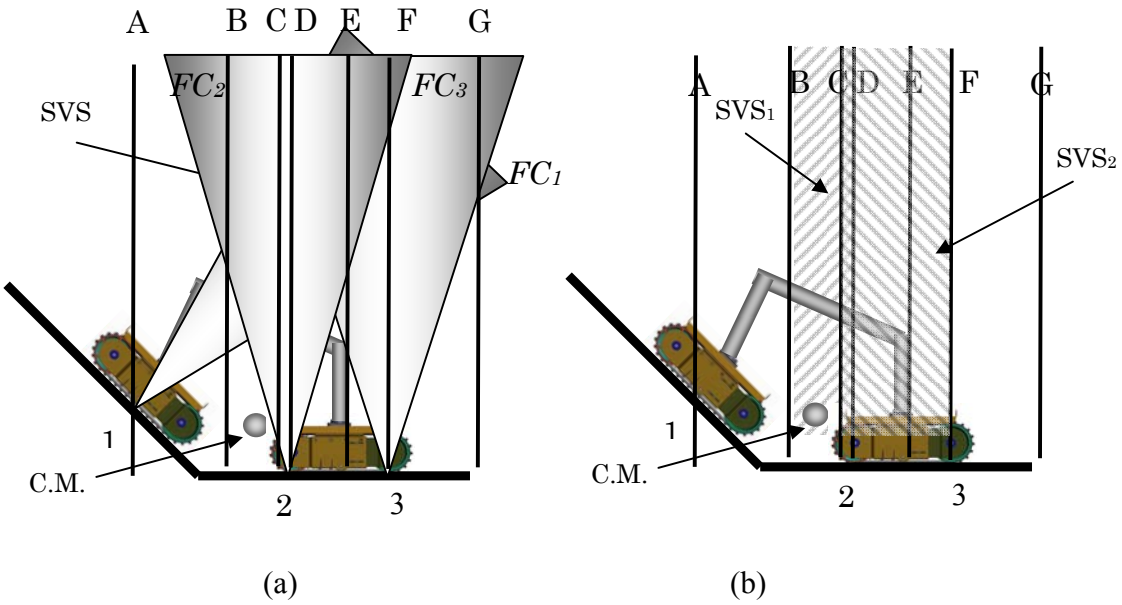

Figure 7: Upper and lower bounds for a single contact of platform #1 and two contacts of platform #2. SVS_1 is constructed between contacts 1 and 2 (vertical lines B and D). SVS_2 is constructed between contacts 1 and 3 (vertical lines C and F). Maximal combined SVS is constructed between vertical lines B and F, and minimal combined SVS is constructed between vertical lines C and D.

Let us define SVS_{ij} as the Stable Vertical Strip constructed by contacts *i* on track #1 and contact *j* on track #2. The location of the center of mass – P_{cm} that guarantees equilibrium for any combination of contact points on the two tracks is therefore given by the intersections of all possible *SVS's*.

$$P_{cm} \in (EVS_{ij} \cap EVS_{ji}) \text{ for all possible } i,j \quad (3)$$

When contact forces are spread evenly along the tracks, the combined *SVS* is given by

$$P_{cm} \in \iint (EVS_{ij} \cup EVS_{ji}) didj \quad (4)$$

which results in the intersection of the two trapezoids shown in Figure 6. Equations (3) and (4) provide upper and lower bounds for the area in which the location of the center of mass can satisfy equilibrium. According to that, the lower bound is between lines C and D in Figure 7, and the upper bound is between lines B and F. A smooth, soft and even terrain indicates that the upper bound (given by (4)) can be applied, while hard and uneven terrain requires the more conservative lower bound given by (3).

A similar analysis is performed for the case where the terrain geometry consists of partially linear **convex** sections rather than the partially linear concave sections shown so far. The analysis is similar to the concave analysis, but the friction cones are now drawn in the negative normal direction as shown in Figure 8. This is justifiable since the friction cones describe the possible line of action of the reaction forces rather than the actual magnitude and direction of the forces. Again, *SVS* is constructed by the intersection of the two friction cones and the position of the contacts. In this configuration the *SVS* is between lines B and C, and the center of mass is outside the strip. As a result, this configuration cannot reach equilibrium and the system is therefore unstable.

Finally, if the robot travels on a flat surface, the centerlines of the two friction cones (or trapezoids) are parallel to each other, and the intersection points between the two cones are at infinity. In such a case, the SVS is constructed between the two contact points.

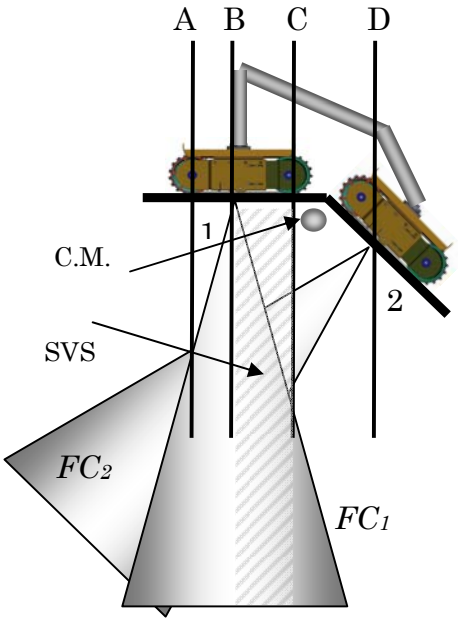

Figure 8. Geometric analysis for a convex surface. Friction cones are pointing in the negative direction to the surface. The rest of the analysis is identical to concave surface.

The analysis presented so far determines possible equilibrium configurations that guarantee stability at a specific location in the terrain. A continuous path of the robot's configurations, that guarantees stable motion from the initial to target position, consists of a series of *SVS's* constructed by possible contacts of the tracks along the path. The simplest motion planner is a linear approximation based on initial and target *SVS's*, which are constructed at initial and target configurations. A line from the center of the initial *SVS* to the center of the target *SVS* determines the required trajectory of the robot's configurations. An odometric model combined with terrain geometry can provide the trajectory of the two tracks for these required configurations. A feasible configuration is one that determines the locations of the two platforms such that the center of mass is on the designated path, and equilibrium is guaranteed along the entire trajectory. If a specific configuration does not guarantee equilibrium, the motion planner must search for an

alternative neighboring configuration. Often, equilibrium is obtained by reducing the height of the center of mass by increasing the horizontal distance between the two platforms. However, geometric, kinematic or external constraints may prevent stable internal configuration for lower center of mass. In such a case, a different configuration of the entire system is required. This is done by searching for the closest position on the next SVS to the current location of the center of mass. When a new feasible configuration is found, a "bypass" is constructed from previous stable configuration to the next stable configuration. Figure 9 shows a path constructed according to this procedure. The dashed line represents the first linear approximation from initial to target configuration between P_0 and P_4. The motion planner detects unstable configuration between P_1 and P_3 due to unreachable internal configurations of the two platforms that guarantees equilibrium. The position of the center of mass is therefore adjusted until a stable configuration is found at P_2, and a stable bypass is constructed from P_1 to P_3 via P_2.

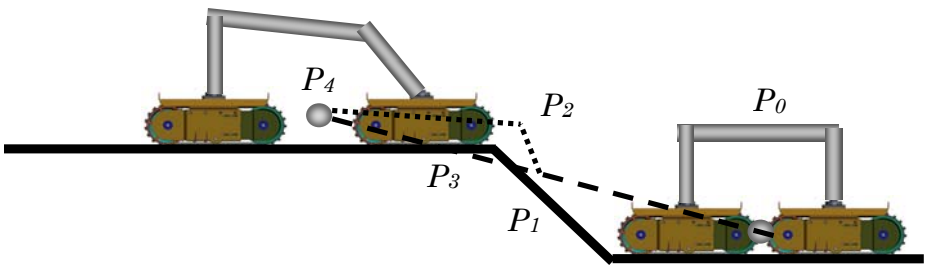

Figure 9: Trajectory from initial to target position. A bypass is constructed for the unstable part of the trajectory (between P_1 and P_3) via P_2.

The length of the connecting beam clearly affects the ability of the robot to negotiate slopes. In general, a longer connecting beam increases the possible stable configurations of the robot. This intuitive fact is expressed by a wider Stable Vertical Strip (SVS), as the

longer connecting beam increases the distance between the contacts. At the first stage, when one platform is on the horizontal surface and the other on the inclined surface, the height that the platform can climb along the inclined surface is proportional to the length of the connecting beam. The length of the connecting beam does not affect the slope angle that the robot can negotiate, as only the coefficient of friction between the robot and ground has an effect on the slope the robot can negotiate. However, if the inclined surface is shorter than length of the beam, the dual platform robot can negotiate slopes that a single platform cannot. Theoretically, a body can maintain equilibrium on an inclined surface with an inclination angle θ and a friction coefficient μ, as long as $\mu \geq tg\theta$. However, the dual platform robot can negotiate much steeper inclinations. For example, a single platform robot with a coefficient of friction of 0.5, can maintain equilibrium on a slope with inclination angles of up to 26.5^{o}. Our stability model shows that the dual platform robot can maintain equilibrium on slopes with similar coefficient of friction, but with inclination angle of up to 63^{o}. However, a longer connecting beam reduces the maneuverability of the robot, particularly in confined spaces and tunnels, as shown in Figure 10. Figure 10(a) shows the robot turning in the confined space of a narrow tunnel. Figures 10(b) and 10(c) illustrate the effect of the connecting beam's length on the maneuverability of the robot in this 90° turn, in terms of the radius of curvature – R_n, and the tunnel's width – W. Both Figures 10(b) and 10(c) show the distance between the connecting beam and the edge of the tunnel. Hence, negative distance represents collision and is practically impossible to maneuver. Figure 10(b) shows that as the radius of curvature increases, the length of the beam can be increased. However, in tight turns the length of the beam must be reduced. In Figure 10(c) the

curvature radius R_n is kept constant at 1m, while changing the width of the tunnel and the length of the beam. As the width of the tunnel increases, the length of the beam can be increased, but when the width is small, the length of the beam must be reduced.

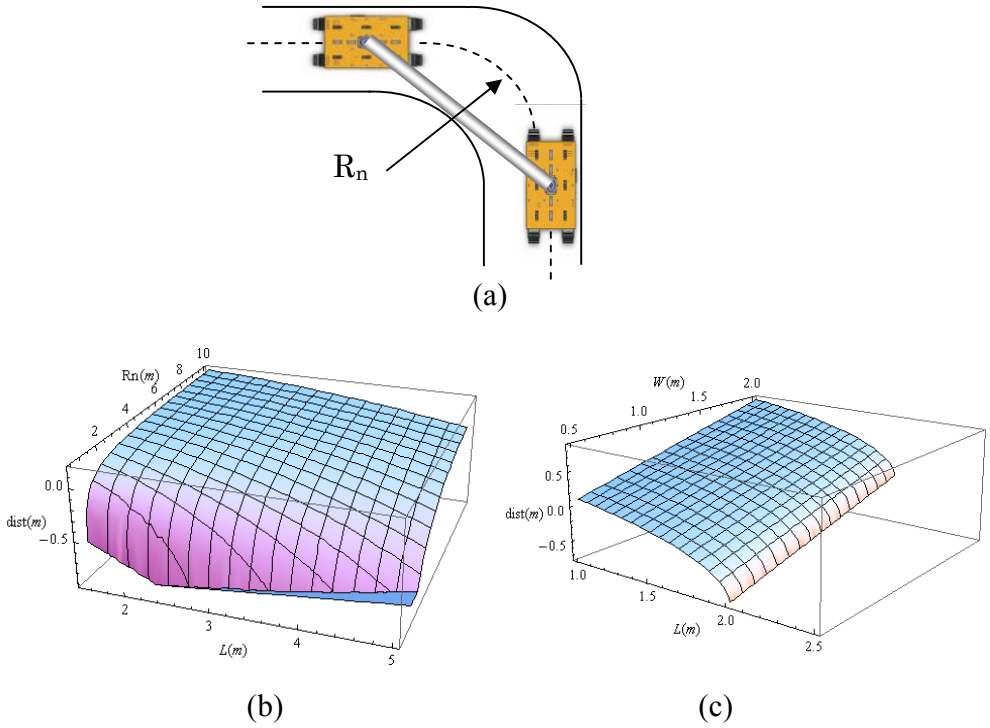

Figure 10: The effect of the length of the connecting beam (L) on the robot's maneuverability in narrow tunnels and pipes, defined by the radius of curvature (R_n), the width (W), and the distance (dist) is the distance between the connecting beam and the inner side of the tunnel. Positive distance means that the robot can move through the tunnel, while negative distance means the robot will collide with the tunnel wall.

IV. Odometric Model and Error Detection

The sensors (potentiometers or encoders) attached to each joint of the connecting mechanism, as well as additional on-boards sensors (inclinometers and gyroscopes) provide sufficient data to accurately and independently determine the position of each joint. Based on this data, a 3D model of the robot's configuration can be constructed to

provide a better accuracy than a conventional odometric system. The position of platform #2 relative to platform #1 is determined using a conventional forward kinematics model given by (5).

$$T_0^7 = T_0^1 T_1^2 T_2^3 T_3^4 T_4^5 T_5^6 T_6^7 = \begin{bmatrix} R_0^7 & d_0^7 \\ 0 \quad 0 \quad 0 & 1 \end{bmatrix}, \tag{5}$$

where each homogenous transformation - T_i^j is composed of a rotation matrix R_i^j and a translation vector d_i^j. The rotation matrix R_i^j is a rotation of the i^{th} coordinate frame at angle θ_i about axis U_i. The translation vector d_i^j is the offset between the i^{th} and the j^{th} coordinate frames. Note that frame 0 is attached to platform #1, and frame 7 is attached to platform #2. A similar model is used for determining the position of platform #1 relative to platform #2, resulting in the following set of equations:

$$T_7^0 = \begin{bmatrix} R_0^{7^T} & -R_0^{7^T} d_0^7 \\ 0 \quad 0 \quad 0 & 1 \end{bmatrix} \tag{6}$$

Once the position of each platform is determined relative to the other platform, odometric errors can be detected according the following procedure:

Define $P_{i,j}$ as the relative position of platform i as determined by platform j. $P_{i,i}$ is the position of platform i according to its own conventional odometric model (using the relative motion of the left and right tracks, and possibly other onboard sensors such as accelerometers, gyroscopes and inclinometers). As previously mentioned, this position estimate is subject to large errors, mainly due to uncontrolled slippage of the tracks, resulting in unbounded positioning errors. If $P_{i,j} = P_{i,i}$ then the two position estimates are

accurate. However, if $P_{i,j} \neq P_{i,i}$, then the odometric model is faulty, and the accurate position of the units must be determined based on a kinematic analysis of the system.

An important assumption is that odometric errors (e.g. slippage) occur only on one track at a time. If two identical odometric errors occur simultaneously, the system may not be able to detect these errors, and the position of the two platforms may be erroneous. However, since the cycle time of the system that determines the position of the vehicles based on the given odometric model is relatively short (<0.001 sec.), we assume that the likelihood of simultaneous errors during this cycle time is small. The kinematic analysis is similar to the one describes by Bornstein (1994) in his *compliant linkage* concept. The compliant linkage provides compliance between the drive wheels or drive axles of a vehicle, to accommodate control errors, which would otherwise cause wheel slippage. However, while Bornstein's implements his compliant linkage by means of a linear bearing that allows relative motion between the front and rear platforms, our complaint linkage consists of the connecting beam, the connecting bars and the six revolute joints, described in Section II.

Figure 11 illustrates the effect of an odometric error on one of the platforms. In the scenario described in the figure, the two platforms are moving to the right on a flat horizontal surface along a nominal straight path, where platform #2 is leading. At a particular instance (Figure 11(b)) the left track of platform #2 momentarily slips, causing the platform to diverge from its nominal orientation. The orientation error of platform #2 is given by $\Delta\beta_2$:

$$\Delta\beta_2 = \frac{\Delta u(2)_l}{w_2} \tag{7}$$

where $\Delta u(2)_l$ is the longitudinal error of the left track of platform #2 due to slippage, and w_2 is the width of platform #2 (the distance between the two tracks). This orientation error is detected by the revolute joint that measures the angle between the connecting bar and platform #2 (θ_1 in Figure 2). This error can also be detected by the gyroscope and accelerometers on-board Platform #2. Notice that at the initial stage there is no lateral error on Platform #2, and the small longitudinal error of Platform #2 – Δl_2 is given by

$$\Delta l_2 = \frac{\Delta u(2)_l}{2} \tag{8}$$

This longitudinal error affects the internal configuration of the connecting beam and bars, and causes the connecting bar of Platform #1 to diverge from it nominal value by $\Delta\alpha_1$ given by:

$$\Delta\alpha_1 = \frac{\Delta l_2}{b_1}, \tag{9}$$

where b_1 is the length of connecting bar of Platform #1. The change in angle $\Delta\alpha_1$ is due to the change of the Euclidean distance between the two platforms, and is detected by the revolute joints θ_4 and θ_5 on Platform #1 and *by* θ_3 on Platform #2. Notice that the connecting bar of platform #2 remains perpendicular to the platform due to the different configuration of the revolute joint θ_2, and that the revolute joint between the connecting bar and Platform #1 (θ_6) is not effected at this initial stage. Also notice that the forward kinematics from Platform #1 to Platform #2 determines that Platform #2 remains at the same vertical level as Platform #1 (using the values of $\Delta\theta_5$, $\Delta\theta_4$ and $\Delta\theta_3$ to calculate the Z coordinate of Platform #2).

In theory, the motion control unit can correct the small orientation error created by the momentary slippage by increasing the speed of the left track or decreasing the speed of

the right track of platform #2. However, if the orientation error is not immediately corrected, and Platform #2 continues its longitudinal motion with the erroneous orientation, a lateral error in the path of Platform #2 – Δt_2 is introduced (Figure 10c). This lateral error affects the internal configuration of the connecting beam, shown by $\Delta\theta_6$ on Platform #1 and is given by:

$$\Delta\theta_6 = \sin\left(\frac{\Delta t_2}{L}\right) \tag{10}$$

where L is the length of the connecting beam. As Platform #2 continues its erroneous motion, the Euclidean distance between the platforms increases until the revolute joints θ_5, θ_4 and θ_3 reach their limits, and the two platforms become one rigid body. Correcting the error at this stage requires a change in the orientation of Platform #2 towards the nominal path and then aligning it back to its nominal orientation.

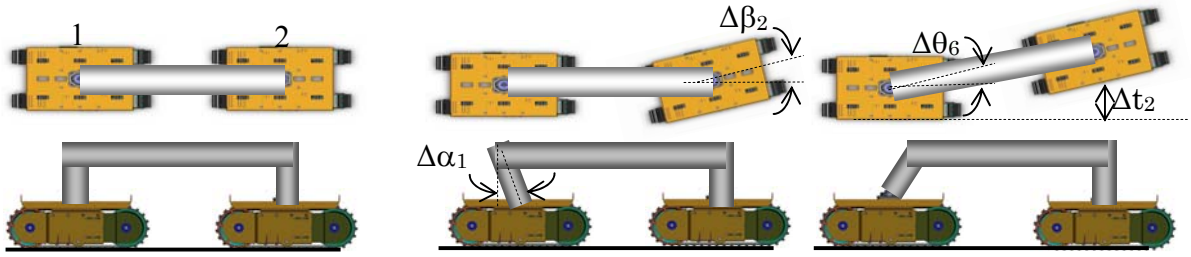

Figure 11: The effect of momentary slippage of the left track on Platform #2. Initially slippage is detected primarily by joint 1 on platform #2 and partially by joints 4 and 5 on Platform #1. If not corrected, the error is also detected by joint 6 on Platform #1.

Figure 12 illustrates the transient response of the momentary slippage of the left track on Platform #2, as shown in Figure 11. The slippage occurs 7 seconds after the beginning of motion, and is immediately detected by θ_1. The slippage causes an initial 5^o orientation error to Platform #2. Since the error is not corrected, a longitudinal error on Platform #2

develops, changing the orientation of the connecting bar on Platform #1 by $\Delta\alpha_1$, which is detected by θ_4 and θ_5 on platform #1 and θ_3 on platform #2 (for clarity we show only $\Delta\alpha_1$). Next, a lateral error develops on Platform #2, which is detected by θ_6. Notice that α_1 decreases for 17 seconds, and then increases until it reaches its motion limit (0.2 rad). This is related to the Euclidean distance between the platforms. At the beginning of the process, the distance between the platforms is smaller than the nominal value due to the loss of longitudinal motion of Platform #2 as a result of the slippage. However, as the lateral error increases, the Euclidean distance increases, resulting in increased value of α_1. A slippage of the right track of Platform #2 will have similar results with symmetric changes on θ_1 and θ_6 and identical changes in θ_4 θ_5 and θ_3.

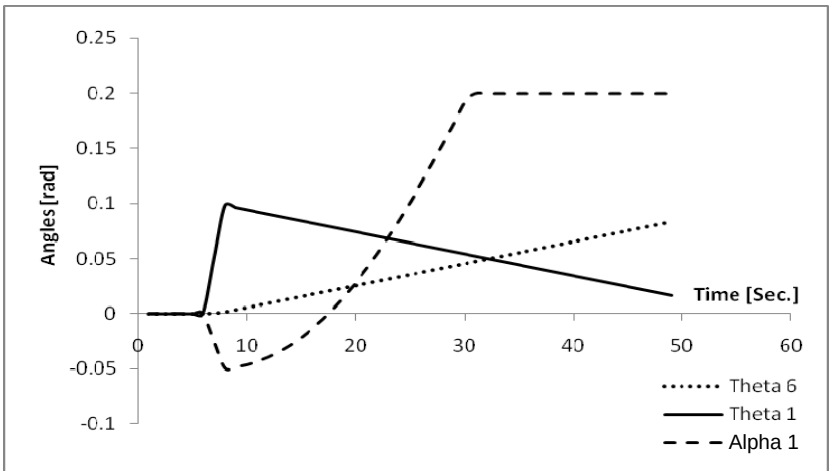

Figure 12: The transient response of momentary slippage of left track on platform #2. Initially θ_1 (on Platform #2) and α_1 (θ_4 and θ_5 on Platform #1) are increased. If the slippage is not corrected, θ_6 on Platform #1 increases until the other joints reach their limit.

A momentary slippage of the right track of the rear platform (#1) will result in a similar relative configuration of the two platforms, as shown in Figure 13. Analyzing the final relative configuration of the two platforms (Figure 13c), without following the transient

behavior, cannot determine which platform initiated the error. However, the transient values of the joints of the connecting mechanism clearly indicate the difference between the two cases as shown in Figure 14. The slippage is immediately detected by the revolute joint between Platform #1 and the connecting bar (θ_6), followed by a change in α_1 and θ_1. Notice the positive value of α_1, due to the fact that in this case the slippage of Platform #1 causes an increase in the Euclidean distance between the two platforms and a monotonous increase in θ_1 (unlike the previous case). These differences in the transient response of the joints, combined with data from on-board gyroscopes and accelerometers, clearly differentiate between the two slippages, which eventually brings the two platforms to a similar relative configuration.

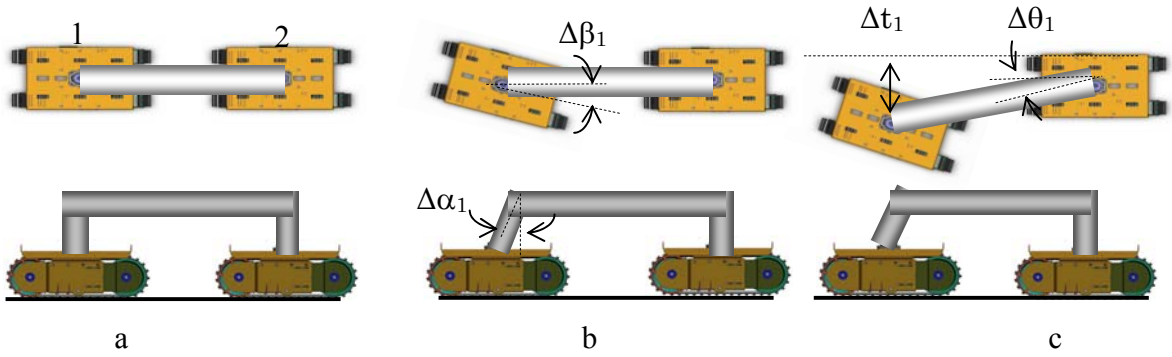

Figure 13: The effect of momentary slippage of the right track on Platform #1, which results in a similar relative configuration between the platforms as in the case of a momentary slippage of the left track of Platform #2.

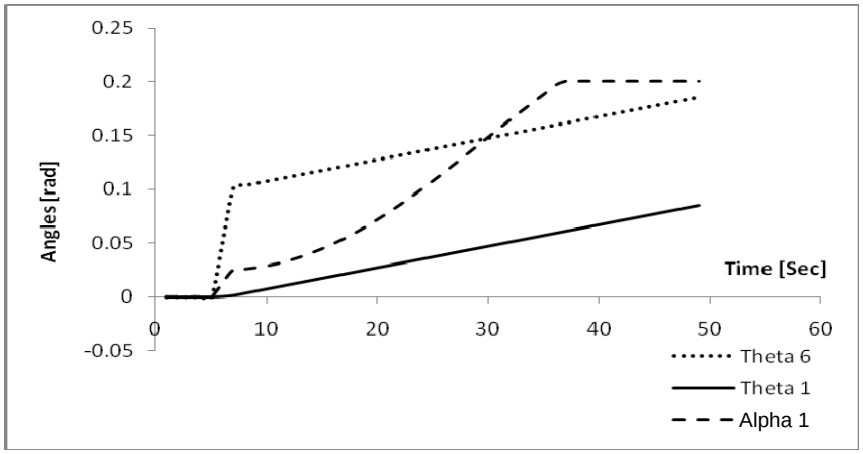

Figure 14: The transient response of momentary slippage of the right track on platform #1. If the slippage is not corrected, the joint angles continue to increase until they reach their linit.

Next, we analyze the case where the robot travels on inclined surfaces or over a bump. For simplicity, we assume partially linear surfaces as we did in our stability analysis. Figure 15 shows the scenario in which the two platforms are moving along a straight path while the leading platform (#1) approaches an inclined surface. The inclined surface first affects the lateral orientation of Platform #1 (Figure 15b), with little effect on the longitudinal position. The effect of the change in orientation of Platform #1 is initially detected by changes in the revolute joints $\Delta\theta_5$ and $\Delta\theta_4$ on Platform #1, and on an inclinometer on-board the platform (if installed). Next, Platform #1 starts climbing the slope (Figure 15c), also affecting the revolute joint $\Delta\theta_3$ on Platform #2. The expression for the inclination angle of the slope - $\Delta\chi_1$ can be derived from the kinematic equations of the connecting mechanism, using the following complex equation (Hunt, 1978):

$$b_2 * e^{(i\frac{\pi}{2})} + L/2 * e^{(i\theta_3)} = r_2 + r_1 * e^{(i\Delta\chi)} + b_1 * e^{(i\theta_5)} + L/2 * e^{(i\theta_4)} \qquad (10)$$

where b_1 and b_2 are the lengths of the connecting bars of Platforms #1 and #2, L is length of connecting beam, r_1 is the distance between the center of Platform #1 and the edge of the slope, and r_2 is the length between the center of Platform #2 and the edge of the slope.

If an inclinometer is installed on-board Platform #2, the inclination angle can be detected directly, once the whole tracks of Platform #2 are on the slope. Notice that the other joints in the connecting mechanism (θ_1, θ_6 and θ_2) are not affected by the change of the lateral orientation of Platform #1 (assuming there are no simultaneous changes in vertical and longitudinal orientations of the platform).

Once the lateral inclination - $\Delta\chi_1$ is detected and determined, the odometric model is updated according to (11):

$$\begin{aligned} \Delta d_h &= \Delta d * \cos(\Delta\chi_1) \\ \Delta d_v &= \Delta d * \sin(\Delta\chi_1) \end{aligned} \qquad (11)$$

where Δd is the total displacement of Platform #1, Δd_h is the horizontal displacement and Δd_v is the vertical displacement. An important feature of the analysis is that once an inclined surface is detected, it is embedded within the local terrain features. This is important since the rear platform (Platform #2) reaches the inclined surface soon after Platform #1 (Figure 15d). This information is then incorporated in the odometric model, and improves the localization accuracy. Notice that once the two platforms reach the inclined surface (Figure 15e), the analysis is identical to the one performed on a flat horizontal surface, subject to the corrections given by (11). Also, notice that when one of the revolute joints reaches its motion limit, it immediately transmits forces and/or moments to the connecting mechanism, and when all three joints reach their motion limit, the whole vehicle performs as a rigid body.

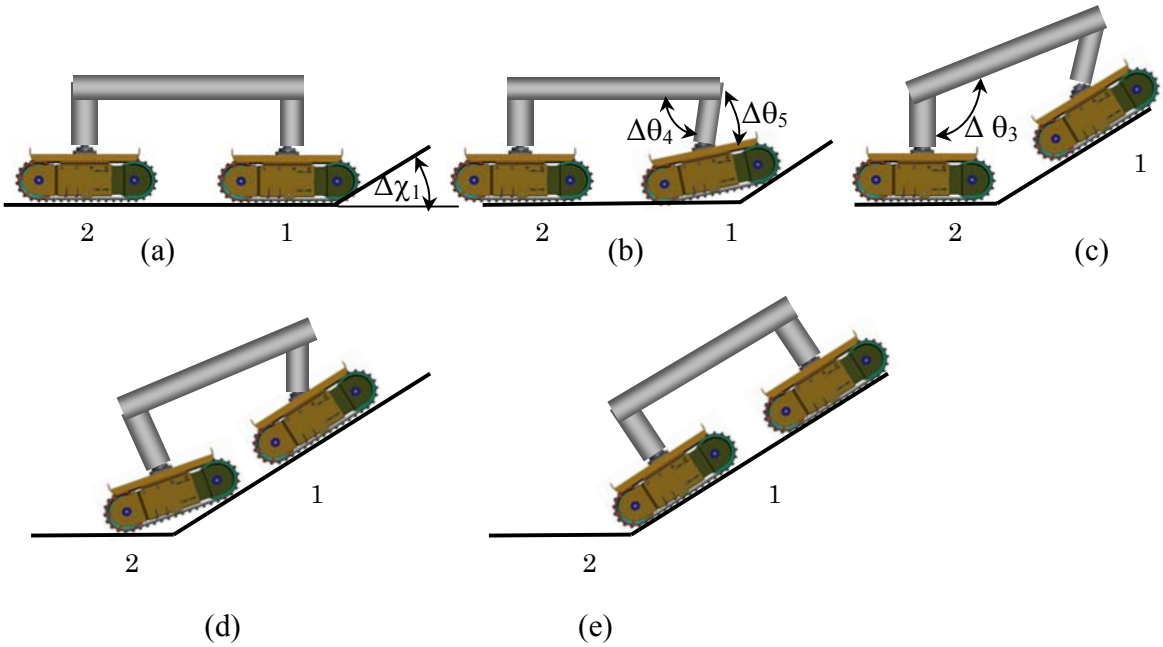

Figure 15: Motion on an inclined surface. Starting with the default configuration (15a) Platform #1 reaches the inclined surface, affecting the relative configuration between the platforms (15b-15d). Once the two platforms are on the inclined surface, the relative configuration between the platforms returns to its original state.

Figure 16 illustrates the transient response of reaching and climbing an inclination of 26° (=0.454 rad) of the three relevant joint. At the initial stage, the two platforms move on the flat horizontal surface with all joints in their intermediate nominal configuration. After 5 seconds, Platform #1 reaches the inclined surface, which results in an immediate and sharp change in θ_5. As motion continues, Platform #1 is entirely on the inclined surface while Platform #2 still moves on the horizontal surface. This results in gradual change of θ_3. When Platform #2 reaches the inclined surface, at t=55 seconds, joints θ_5 and θ_3 detect this stage with a sharp change. Finally, when Platform #2 is entirely on the inclines surface, all angles return to their initial values, and the connecting mechanism is identical to its original configuration on the horizontal surface.

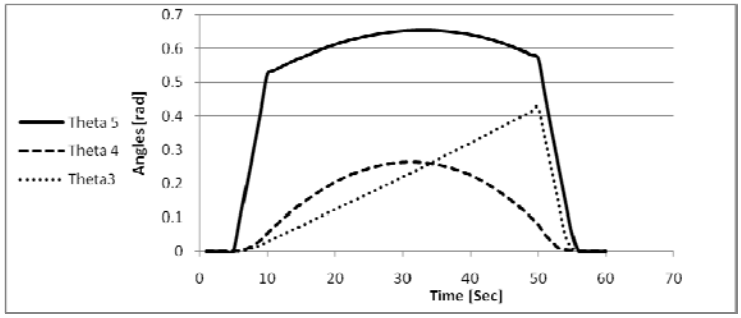

Figure 16: The transient response in motion over inclined surface. Only the relevant joint angles of the connecting mechanism are affected (θ_3 on Platform #2, and θ_4 and θ_5 on Platform #1). Once the two Platforms are on the inclined surface (55 sec. from the beginning of motion) all angles return to their initial values.

As shown in the case of a lateral slippage, the length of the connecting beam also has some effect on the localization performance when traveling over an inclined surface. The sensitivity of the connecting mechanism to detect odometric errors increases as the length of the connecting beam is reduced, as shown in Figure 17. The figure shows three transient responses for lateral slippage with various lengths of the connecting beams: 20cm (a), 100cm (b) and 200cm (c). While α_1 is not affected by the length of the connecting beam, θ_1 and θ_6 become more sensitive to the odometric error as the length of the connecting beam is increased. A longer connecting beam requires more sensitive encoders or potentiometers on the revolute joints in order to maintain similar level of accuracy. For example, a connecting mechanism with a 100 cm long beam and an angular encoder with a resolution of 500 PPR (pulse per revolution), can detect relative lateral or vertical errors larger than 1.26 cm between the two platforms. A connecting mechanism with a 200 cm connecting beam and a similar encoder resolution can detect odometric errors larger than 2.52 cm.

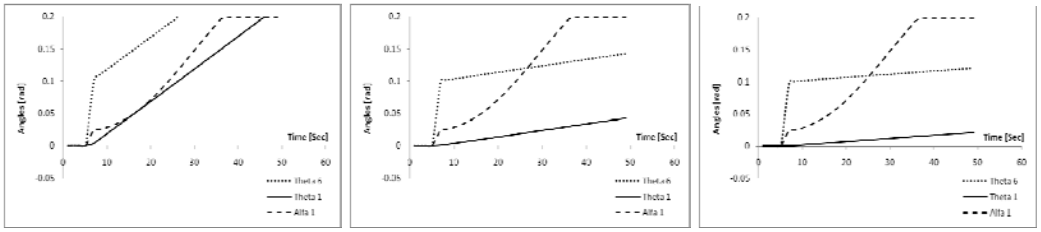

a b c

Figure 17: The sensitivity of the odometric model as a function of connecting beam's length (a-20cm, b-100cm, c-200cm). A longer connecting beam reduces the sensitivity of the system in the detection of odometric errors due to slippage of one platform.

V. Control and Motion Planning

Two local motion controllers perform the low-level motor control on each platform. Currently we use high power controller (RoboteQ AX2550) that can provide 12V and up to 120A to the driving motors (http://www.robotmarketplace.com/products/RTQ-AX2550.html). These controllers are required in order to control the speed of each driving motor and provide sufficient power in challenging scenarios, in particular when one robot is required to assist the other. The local controllers are connected to a higher-level controller (a laptop), which synchronizes the two local controllers according to the odometric model described in the previous section, and the updated data from the connecting mechanism. The higher-level controller also performs the stability analysis described in Section III. Given the mission and the updated configuration of the system, the higher-level controller generates the required trajectory of each tracked platform, monitors the performance of the system, and if required, updates commands to the local motion controllers.

There are four operation modes implemented in the system:

1) **Single mode** – in this operation mode, each platform is controlled independently, subject to the mechanical constraints of the joints on the connecting mechanism. This mode is useful for motion on terrains where no specific configuration between the two platforms is required, or when one platform assists the other to overcome obstacles along the trajectory (e.g. when one platform experiences difficulties it cannot negotiate on its own). In this operation mode, the connecting mechanism is particularly useful for transferring forces and moments between the two platforms according their relative configuration. This mode can be operated manually, using dual joystick device, or automatically using heuristics according to pre-defined scenarios (e.g. climbing over a steep inclination, assisting a failed platforms etc.).

2) Twin mode – In this mode, the two platforms perform identical motion pattern. The higher-level controller transmits identical motion commands to the local controllers of each platform. Theoretically, the two platforms remain parallel to each other (or collinear) during this operation mode. If one platform deviates from the desired position (e.g. due to slippage), this deviation is immediately detected and corrected. This mode is efficient when the whole system is used as an Omni-directional robot, or when changes in the internal configurations of the units are not required. It should be noted that the orientation of the connecting mechanism remains constant in this operation mode regardless of the motion of the two platforms as shown in Figure 18.

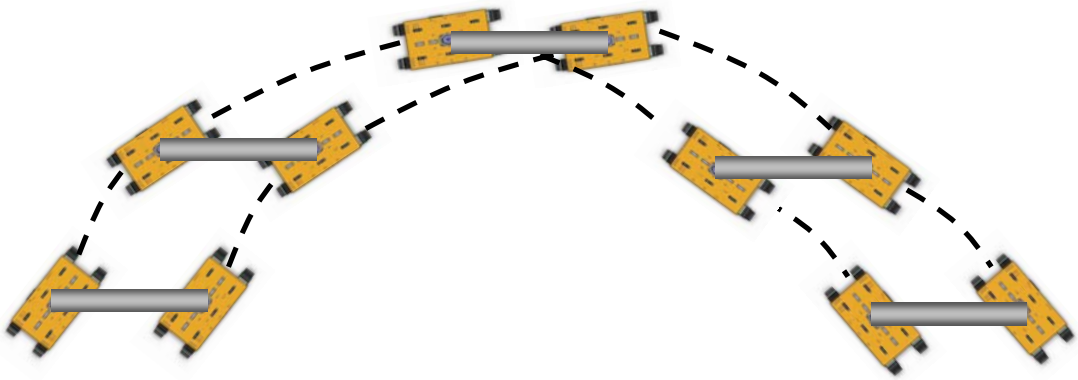

Figure 18: The "Twin" mode. The two platforms perform identical motion pattern, and theoretically remain parallel to each other. Also, the orientation of the connecting beam remains constant.

3) **Follow mode I**– in this operation mode, the rear platform follows the front platform such that the trajectories of the rear tracks overlap the trajectory of the front tracks. This mode is particularly useful for motion in long and confined spaces such as tunnels and tubes where the width of free passage is limited. The higher-level controller determines the trajectory of the front platform, and then sends commands to the rear controller to follow this trajectory. Again, when the rear platform deviates from the required trajectory, the joint sensors of the connecting mechanism, and possibly other on-board sensors detect the deviation and the higher-level controller corrects it. This mode can be operated automatically, where the trajectory of the front platform is determined according to an external motion planner or according to sensory data (e.g. for obstacle avoidance). However, this mode is also efficient for manual operation of the robot as the operator is required to control the front unit only, while the higher-level controller determines the required motion of the rear platform. As mentioned, the Follow mode I is particularly useful for motion in tunnels and confined spaces, as shown in Figure 19. In this figure, Platform #1 leads the motion

inside a narrow tunnel using laser sensors that guide the platform to the center of the tunnel, while Platform #2 follows its trajectory.

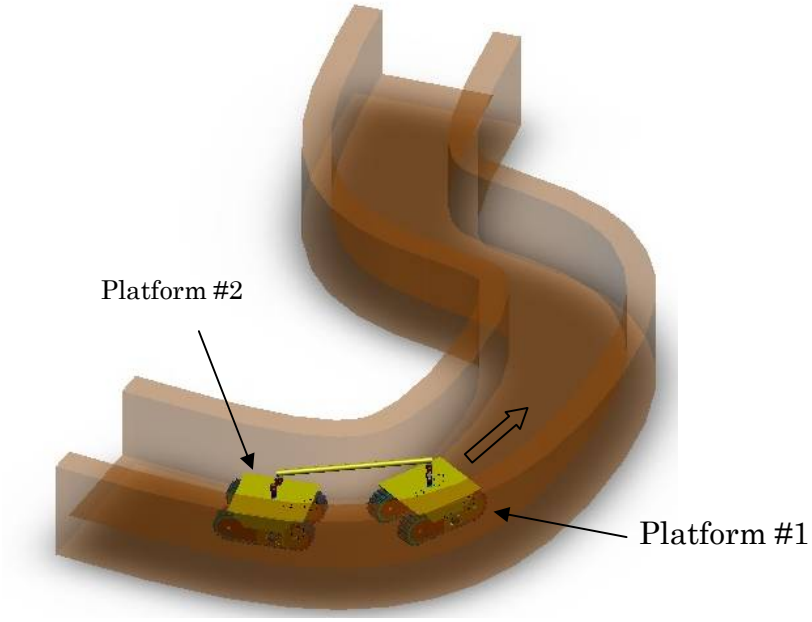

Figure 19: Follow mode I inside a narrow tunnel. The rear platform accurately follows the route of the leading platform.

4) **Follow mode II** – this mode is similar to the previous mode (Follow mode I), where the rear platform follows the front platform. However, in this mode the rear platform continuously aligns itself with the connecting beam. This is useful when devices mounted on the rear platform (camera, mechanical arm etc.) must follow the center of the front platform. Another application that can benefit from this mode is when maximum force transmission from the rear platform to the front platform is required. In this case, the full dragging force of the rear platform is transferred along the connecting mechanism to the front platform with minimal loss, as illustrated in Figure 20. In the configuration shown in Figure 20(a), only part of the force ($F\cos\theta$) is transmitted, while in the configuration shown in Figure 20(b) all the force is transmitted.

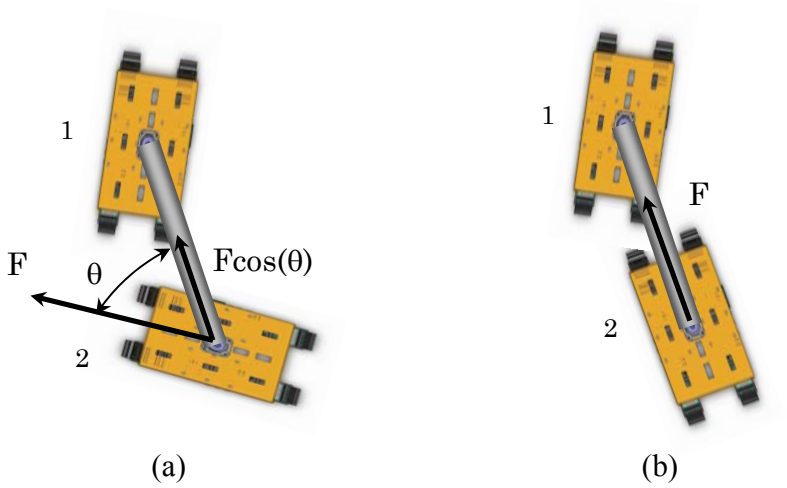

Figure 20: Force transmission in Follow mode II. While in the general configuration only part of the force is being transmitted from Platform #2 to Platform # 1 (20a), the full force is being transmitted when in Follow mode II (20b).

VI. User interface

The control software allows the operator to control the system manually, using a dual joystick that provides the user with all options to control the two platforms. In the single mode, the user can control each platform independently using one handle of the dual joystick for each platform. In the other operation modes, the user can control the front platform, while the higher-level controller controls the rear platform. The user can also select the "auto" mode in which all operations are determined by the higher-level controller according to the specific mission and the sensory data. For example, for motion in tunnels or tubes the robot is required to move in the center of the tunnel using its on-board laser range finder.

A graphic user interface (GUI) displays the various operation modes, internal data (sensors data and winch status), a map of the robot operation area and an overlaying graph of the robot's trajectory and current position, and a video image from the on-board camera, mounted on the front platform. Additional data can be presented using special

commands. In addition, a graphic window shows a 3D scheme of the relative internal configuration of the two platforms. This assists the operator to comprehend the updated robot configuration even without direct eye contact with the robot. Figure 21 shows the GUI.

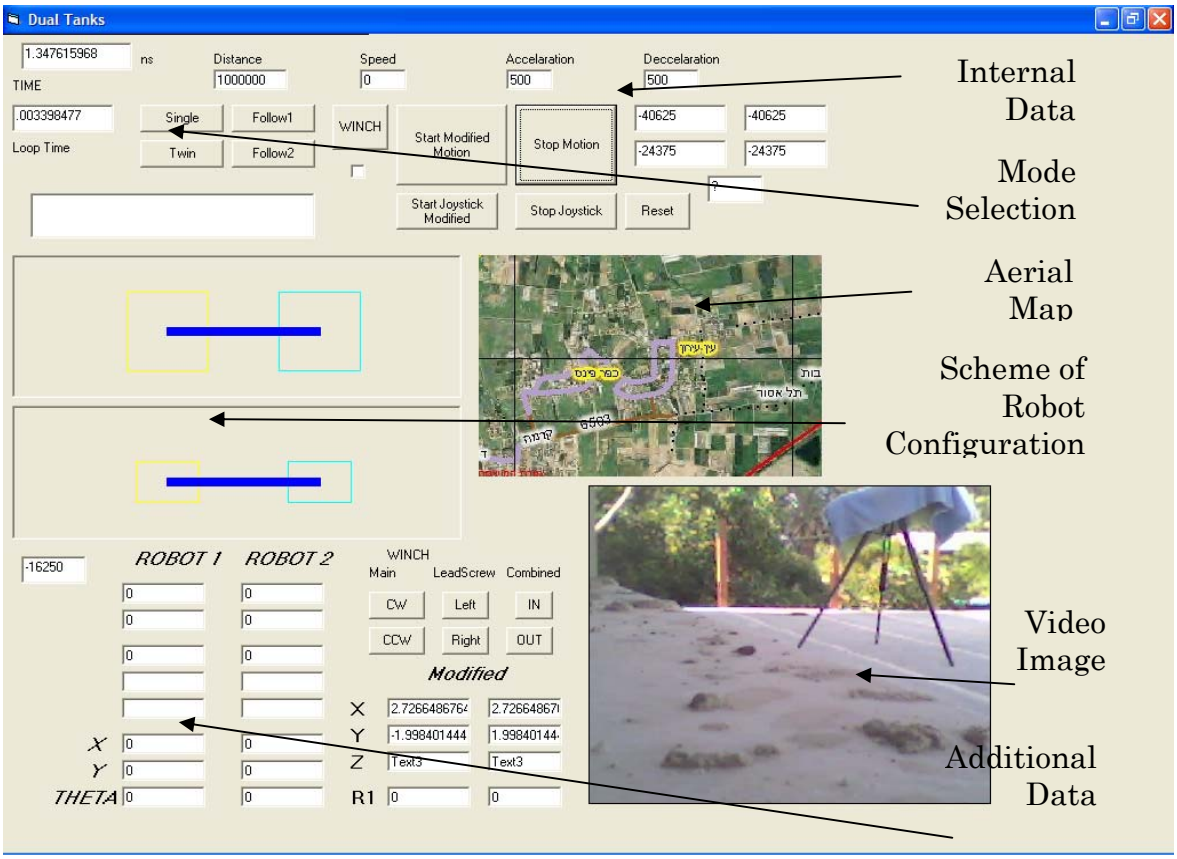

Figure 21: The Graphic User Interface (GUI). In addition to the updated platforms' location in 3D, it provides the user with a graphic scheme of the platforms' relative configuration, the state of all joints angles, a video image from the leading platform, and an overly of the robot location on an aerial map (when operating in underground tunnels or tubes).

VII. Experimental results

In this section we describe experimental results conducted using a simulator and our dual-track robot prototype. We first describe the mobility experiments and capabilities of a single platform robot. Then we describe the mobility experiments and capabilities of the dual-track configuration. Finally we describe the odometry system experimental results.

Most of the experiments described in this section are shown on a video that can be downloaded from: http://www.bgu.ac.il/~ashapiro/media/dual-track_robot.wmv

Single platform mobility experiments

Each single robot (Figure 22) is composed of two tracks, a metal plate that interconnects the tracks, two 12V batteries mounted underneath the plate between the two tracks, and a controller and driver mounted on top of the plate (not shown). In the figure, the lower part of the connecting mechanism is left attached to the robot. The total weight of the robot is 25 Kg. The size of the robot is: length – 54cm, width – 36 cm, height (without the connecting mechanism) – 30cm. The robot is designed to carry a nominal payload weight of 30Kg. However, our experiments on a horizontal paved surface shows capabilities to carry a maximal payload of over 100Kg , and to generate a drag force larger than 150Kg.

Figure 22: The single robot platform prototype. Dimensions: 54x36x30cm (LxWxH). Weight: 25 Kg. Maximum payload: 100 Kg. Maximum drag force on flat surface: 150 Kg. Speed without load: 80 cm/sec. Speed with maximum load: 50 cm/sec.

The first set of experiments aims to measure the robot's velocity with various payloads and on different terrains and slopes. We first let the robot travel for a distance of 18m on a horizontal paved surface with 30Kg payload. The robot achieved an average travel speed of 59cm/sec with a S.D. of 2.54cm/sec. The second experiment was an upwards motion on an inclined surface, again with a 30Kg payload. The robot was able to climb a 35˚ slope at an average speed of 30.3 cm/sec with S.D. of 1.75cm/sec. In additional experiments with steeper slopes of 44˚, 50˚ and 60˚, the single robot did not manage to climb the surface due to slippage of the tracks. This result is predictable, as the theoretical friction coefficient between the robot and the surface (rubber and wood) is 0.62, which indicate that the maximum possible inclination is 31.8˚. The larger slope angle that was obtained in the experiments is probably due to the tracks geometry and small variations in the surface texture. Next, we examined the single robot's capability to negotiate steps. The robot was able to climb up steps with height of 12cm each, carrying a load of 30 Kg. The robot failed all the tests with larger step height.

We further checked the robot mobility on dry and wet sand dunes. While carrying a payload of 30Kg, the robot was able to climb up 15˚ slope of a soft sandy hill for a distance of about 30 meters. The single robot was able to climb up 30˚ slope of a soft sandy hill, but only for 15 meters. At this stage we noticed that much sand was accumulated between the driving gears and the tracks, resulting in high tension of the suspension mechanism and the rubber track. As a result of these experiments, we improved the track and suspension mechanism design, and added a cover that prevents some of the sand accumulating between the driving wheels and the track. These

improvements allowed the robot to travel larger distance on sand dunes, but in all experiments, the robot eventually dug itself into the sand, and could not release itself.

Dual-track robot mobility experiments

We measured the velocity of the dual-track robot (Figure 23) while traveling a distance of 18m at full speed on a horizontal paved surface. The robot's payload was 30Kg on each platform (total of 60Kg). The average velocity was 53 cm/sec with a S.D. of 1.2cm/sec. This is a little slower (10%) than the single robot experiment. The reason for this difference is that the two robots were required to coordinate their speeds in order to maintain the required internal configuration according to the *Follow 1* operation mode. This coordination requires one platform to adjust its speed when the other platform confronts mobility challenges. Although the experiment was conducted on a flat horizontal paved surface, the small variations of the surface texture, and imperfections in the surface geometry resulted in slower speed of one platform that was adjusted by the other platform's speed.

Figure 23: The dual-track robot platform prototype. Range of the connecting beam length: 0.5-1.5 m. The robot is capable to climb a 60° slope with a payload of 60 Kg.

In the next set of experiments, we investigated the transition of the robot from a horizontal plane to an inclined plane, such that the rear platform pushes the front platform forward (similar to Figures 5, 6, 7 and 9). All these experiments where conducted in the laboratory environment on wooden inclined surfaces with a theoretical friction coefficient of 0.62. The following table summarizes the result of these experiments when the robot carries a payload of 60Kg.

Table 1: Velocity of dual-track robot while climbing a slope

slope	Travel distance	velocity	S.D
35˚	121cm	28.8cm/sec	9.8cm/sec
44˚	121cm	28.6cm/sec	10.4cm/sec
50˚	121cm	24.3cm/sec	8.3cm/sec
60˚	121cm	11cm/sec	9.6cm/sec

As shown, the dual-track robot is capable of climbing a 60˚ slope, compared with the single platform robot that could climb a 35˚ slope on a similar surface. As shown in the previous sections, in the dual-track configuration the platforms help each other by transferring forces through the connecting mechanism. The results obtained in this set of experiments were verified using numerical simulation. Our simulations for the dual-track robot indicate a theoretical maximal climbing slope of 63.65˚. The actual climbing slope of 60˚, shown in Table 1, is therefore, expected, and matches the numerical theoretical computation. Figure 24 presents the theoretical maximal climbing slope for a single and the dual-tracked robots as a function of the coefficient of friction. This graph clearly indicates that advantage of the dual-tracked robot in climbing steeper slopes, compared with a single robot. On average, the dual tracked configuration increases the possible slopes the robot negotiate by 50%

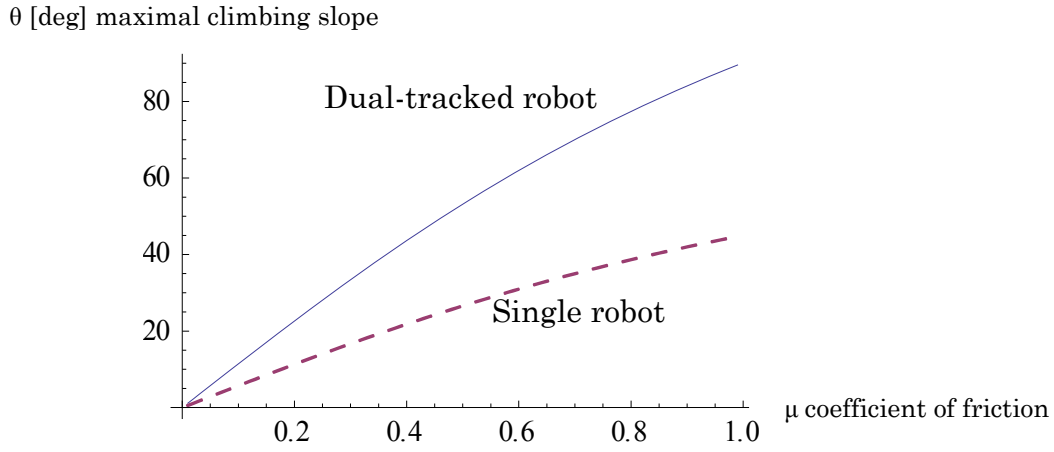

Figure 24: The theoretical maximal climbing slope angle vs. the coefficient of friction for a single robot and for the dual-tracked robot. On average, the dual-tracked robot can climb up slopes twice as steep as compared with a single tracked robot. Experimental results verified the theoretical estimates.

The following set of experiments verifies the robot's capabilities to detect bumps and holes along the trajectory, and to estimate the slope angle of inclined surfaces. In these

experiments, the robot is traveling along a straight line. Along this line there is a small bump, and then an inclined surface, where the inclination angle can be adjusted. Figure 25 shows the results of two experiments. Figure 25(a) shows the experiment with a 26° slope and figure 25(b) with a 18° slope. The graphs show the values of the six encoders attached to each revolute joint on the connecting mechanism (E_1-E_6) and the slope estimate based on these encoders' values. Note however, that we mounted the encoder that measures θ_5 (i.e. E_5) in the opposite direction to that described in figure 2. Hence E_5 measures $-\theta_5$ instead of θ_5. The slope estimation is based on the kinematics of the system. The robot reaches the bump about 3 seconds after the beginning of motion, and start moving on the inclined surface about one second later. The bumps and the inclined surface are mainly detected by changes in E_3, E_4 and E_5 (measuring the revolute joints θ_3, θ_4 and $-\theta_5$ respectively), with little or no effect on the other joints. Therefore, in this experiment the slope estimation is reduced to the planar case where the slope angle equals $\theta_3+ \theta_4+ \theta_5$. In the 26° slope experiment the robot estimates a slope value of 26.3° (an error of 1.2%), and in the 18° slope experiment the robot provides an estimate of 18.7° (an error of 3.8%). In the experiments, E_4 almost equals E_5. This is due to the controller, which changes the robot velocity in order to maintain the link between joints 4 and 5 perpendicular to platform #2. Therefore, this link is almost perpendicular to the slanted surface and it means that the surface slope angle is measured mostly by E_3. Unlike the case which is shown in figure 16, here the robot does not climb all the way up, but only the front platform climbs the inclined surface while the rear platform remains on the horizontal surface. Another difference is that here the user controls the motion of the rear platform (#1) while the front platform (#2) adjusts its' velocity in order to maintain

the link between joints 4 and 5 perpendicular to platform #2, while in the experiment shown in figure 16 the two platforms maintain constant speed.

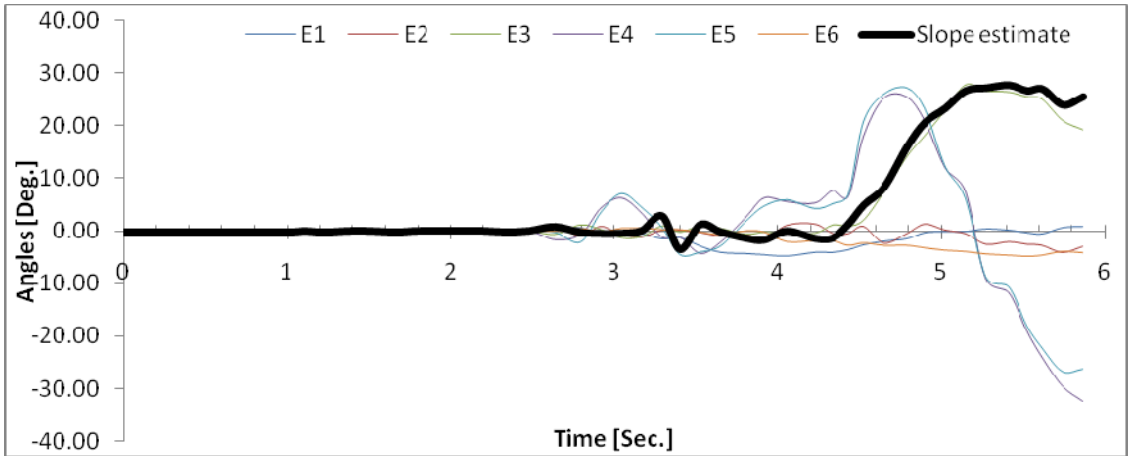

(a)

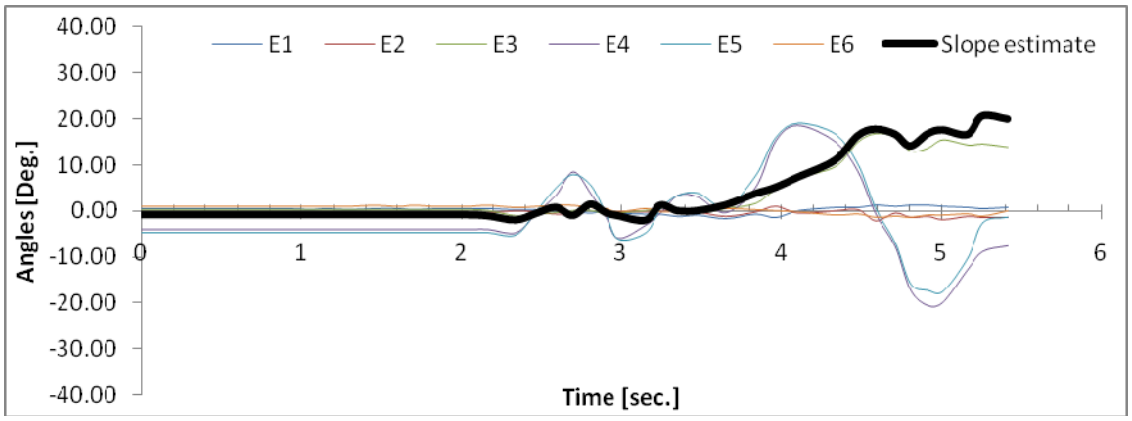

(b)

Figure 25. Encoders values and slope estimate for motion along a straight line with a bump and an inclined surface of 26° (a) and 18° (b).

In the next set of experiments, we tested the robot capabilities to climb steps while carrying a heavy load. The dual-track robot was able to climb up steps of 12cm carrying weights of up to 90 Kg. The robot failed climbing steps of 14, 16 and 18cm (the standard height), and in fact did not show an improvement over the single platform robot. This failure is due to the low attack angle (the angle between the front track and the surface).

This is a well-known limitation of tracked mechanism, that can be modified either by changing the attack angle using a different suspension configuration, or by using an additional mechanism (e.g. flippers) such as the one in the 510 PackBot robot by iRobot. Next, we conducted experiments on various types of terrains, including low bush terrains, rocky, wet and dry sand dunes. The robot was able to climb up 30˚ slope hills of rocks, soft sand and wet sand while carrying a total payload of 60Kg. Unlike the single robot that failed climbing the sand dune after 15 meters, the dual platform robot managed to repeatedly climb the entire 30 meters of sand dune. In these experiments we used the manual single mode, and managed to recover a troubled platform using the other platform and the connection mechanism. However, we observed difficulties in sandy slopes steeper than 35^0, as both platforms had a tendency to dig themselves in the sand. In the final experiment we inserted the robot into a 15m long tunnel. The robot managed to travel in the middle of the tunnel in the follow 1 mode, using its on-board laser range finders. Figure 26 shows the dual-track robot successfully climbing a rocky hill with a steep slope of 30˚.

In experiments conducted inside sandy horizontal tunnels, similar to the one shown in Fig. 19, the dual tracked configuration allowed the transfer of up to 200Kg load (a load to weight ratio of 4:1) in narrow passages (width of 50cm), that conventional vehicles in that size range cannot traverse.

Figure 26: The dual-track robot climbing up a 30° slope of uneven rocky hill. In experiments conducted on sand dunes the robot was capable to climb 35° sloped while carrying 60 Kg payload.

Odometry experiments

Based on the combined odometry system presented on Section IV, we now present the experimental results of the system in terms of motion accuracy. In these experiments, the robot was commanded to pass through predefined waypoints while traveling on uneven terrain consisting of sand and gravel. When the robot arrived to a waypoint it stopped, and its location was measured manually, and compared with the location determined by the odometric model. The waypoints were marked on the ground using a colored tape, and the measurement was done manually using a measuring tape. Table 3 and Figure 27 summarize these experimental results.

Table 3: Results of path following experiment.

Reference Points [m]		Experiment 1			Experiment 2			Experiment 3		
X	Y	X	Y	Error [%]	X	Y	Error [%]	X	Y	Error [%]
7	3	7	3	0	7	3	0	7	3	0
2	7	2.2	7.1	3.5	1.9	7	1.5	2.1	6.8	3.6
4.5	9	4.3	8.9	2.5	4.25	9.2	3.3	4.4	9.5	5.2
7	7	7.2	6.8	2.2	7.05	6.75	1.9	6.9	6.85	1.3
2	3	2	3.3	1.6	2.05	3	0.9	2	3.2	1.0
4.5	1	4.6	1.1	0.6	4.35	1.2	1.1	4.7	0.9	1.0
7	3	7.1	2.9	0.5	7.3	2.9	1.2	7.1	3.2	0.8

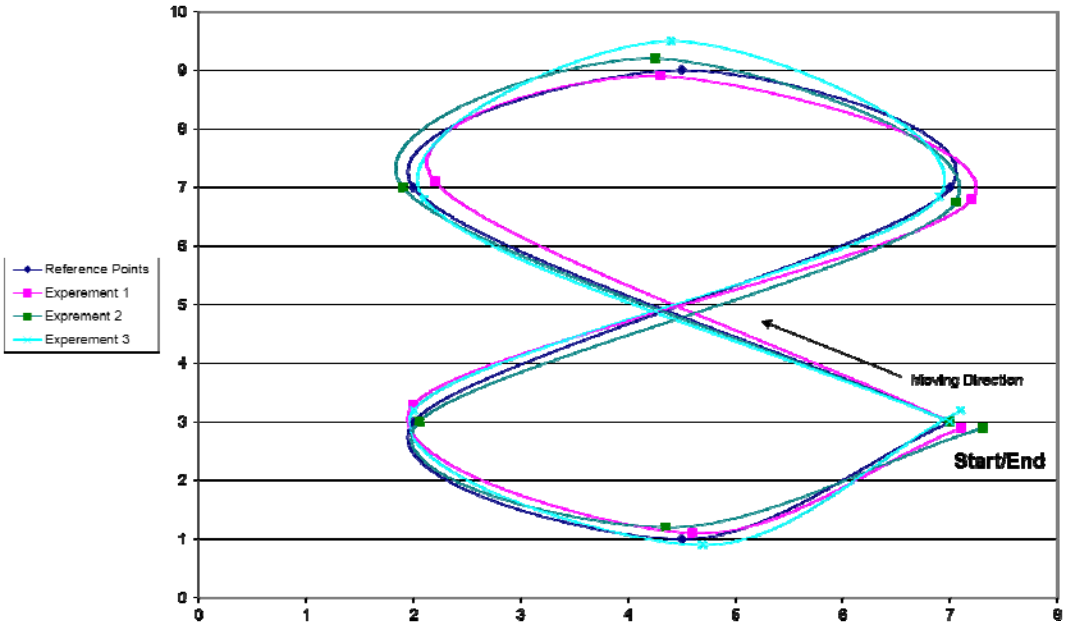

Figure 27: Motion path of the dual-track robot when commanded to pass through waypoints along a 8 shape trajectory. The average location error is 2% for a 26 m travel.

The results of these experiments show that the robot managed to accurately pass through the given waypoints. After traveling a distance of 26m at each experiment, the robot was able to reach the given waypoints with an average error of less than 2%. Moreover, the maximal error was only 5.23% of the travel distance. These experiments verify our assumption that most odometric errors do not occur simultaneously (and therefore can be corrected), and show great feasibility of using the dual-odometry based localization

system for mapping outdoor terrains where no external position system (e.g. GPS, triangulation, triatelation etc.) is available. This is particularly practical in underground tunnels, pipes, tubes and caves where communication with external devices is limited or not possible.

The next set of experiments illustrates the robot's capability to detect and recover from odometric errors during motion. In these experiments, one of the platforms is intentionally subjected to external disturbance (external force that drags it away from its nominal trajectory) during motion. Figure 28(a) shows a global view of the robot's trajectory from its initial to final configuration. In the middle of its motion (about 6 seconds from the beginning), the rear platform is dragged from its nominal trajectory for 0.5 seconds, as illustrated in 28(b). Once the platform is released, the control system, that detects this error, guides the rear platform back to its nominal trajectory. Figure 28(c) shows the angles of the revolute joints of the connecting mechanism during this process. As discussed in Section IV (and shown in the simulation results), the odometric error is immediately detected by θ_1 and θ_6 (E1 and E6 in the figure), with smaller changes on the other joints. Notice the oscillations of the other angles around the origin. These oscillations are due to the control system, trying to maintain the platforms at their nominal configuration. Tuning the control gains can adjust these oscillations.

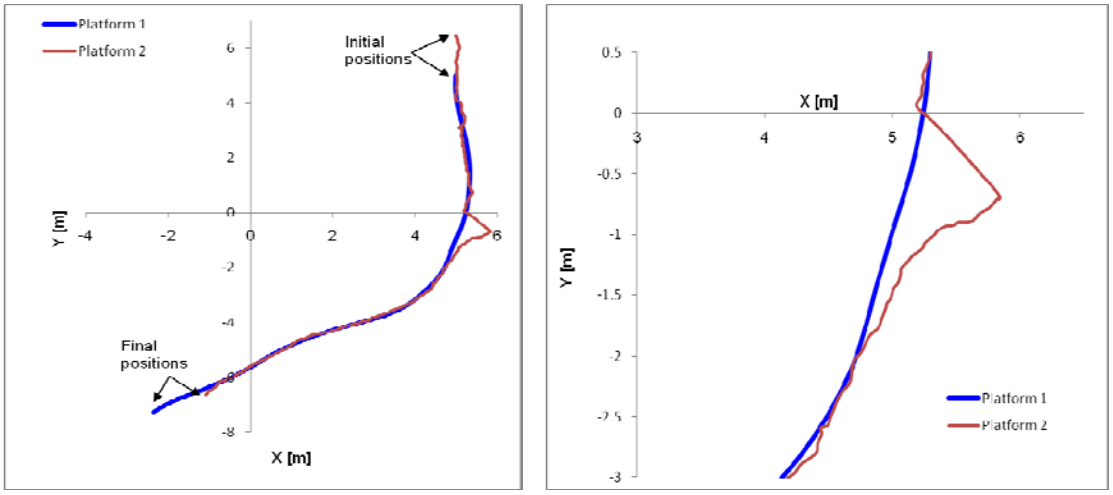

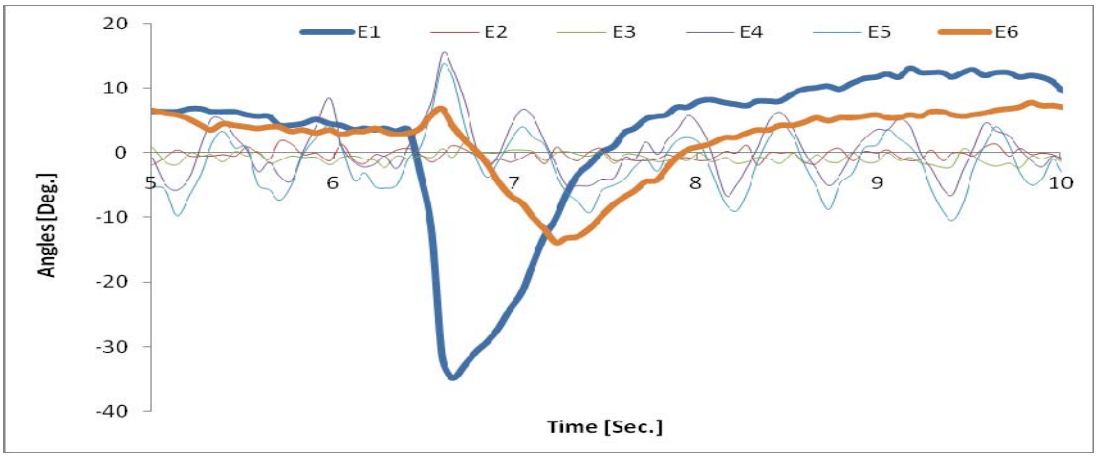

(c)

Figure 28. Robot's capability to detect and recover from odometric errors during motion. The rear platform is subjected to external disturbance deviating it from it nominal trajectory (26(a) ad 26(b)). The error is detected by the revolute joints θ_1 and θ_6 (26(c) and corrected by the control system.

Finally, figure 29 shows an experiment of the robot running under Follow 1 mode. As shown, the rear platform closely follows the front platform, using the encoders' values of the connecting mechanism. This experiment was conducted in real outdoor environment using its on-board devices. As with the previous experiments, the two platforms reach their final configuration with minimal deviation from the nominal trajectory, while continuously recovering from possible odometric errors during motion. Notice how the

control unit maintains the values of the revolute joints with only small deviations from the nominal values.

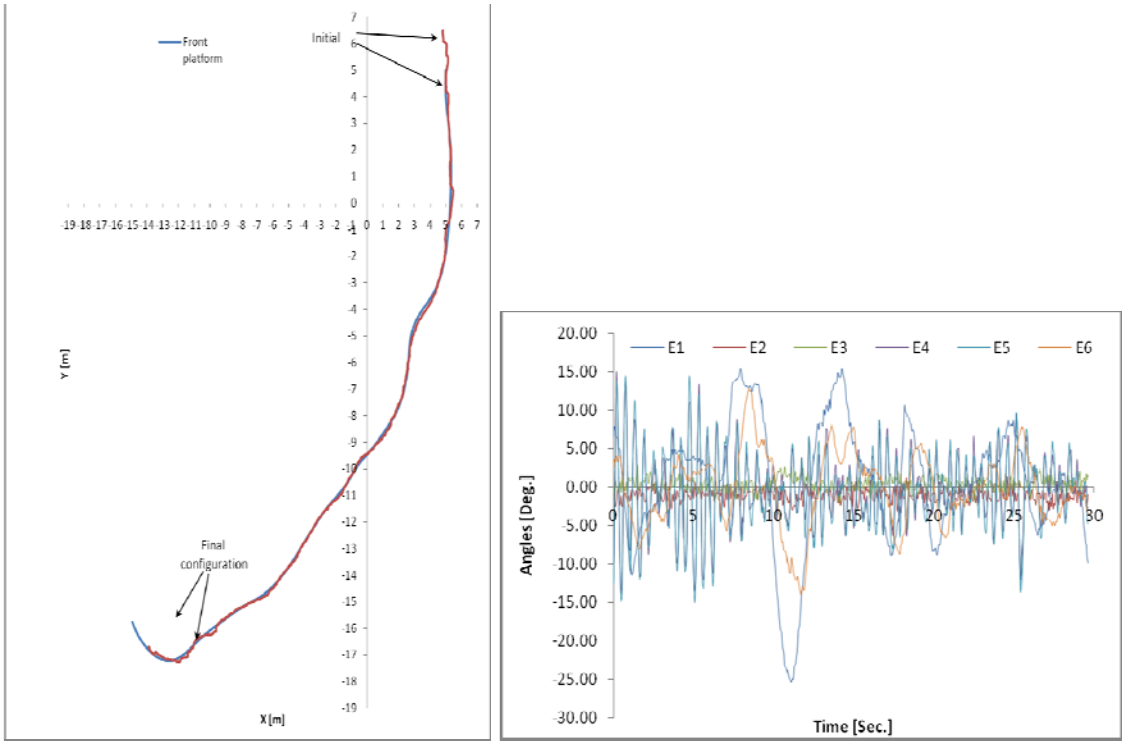

(a) (b)

Figure 29. The trajectories of the two platforms running in Follow 1 mode (29a), and the values of the six revolute joints of the connecting mechanism (29b).

VIII. Summary

In this paper we presented a concept of connecting two tracked platforms with a novel connecting mechanism. The mechanism allows a relative 6 DOF motion between the two platforms using 6 revolute joints. Sensors attached to the revolute joints measure the configuration of the connecting mechanism. The joints are configured such that they allow independent motion for each platform while they are within the designated range. However, the connecting mechanism can also be used for forces and moments transmission between the two platforms. This is achieved when the joints approach their

motion limit. Hence, when encountering rough terrain or steep slopes, the platforms can help each other to overcome the challenges. We showed the geometric conditions for the robot to maintain a stable equilibrium. Stability analysis (as well as experimental results) shows that the robot can operate on extreme slopes 50% steeper than a single robot can. We also presented an odometric model for the dual-tracked robot. The odometric system is based on the fact that each robot has its own odometric system. We use the seemingly redundant information on the internal configuration of the two robots, measured by the sensor on the connecting mechanism. This redundant information is used for correcting odometric errors that may occur, and results in an autonomous accurate dead-reckoning. We conducted an extensive set of experiments with both the single platform and the dual tracked robots. The experiments show that the dual-tracked robot concept has better mobility capabilities on rough and challenging terrains. The robot is able to climb slopes that are 50% steeper than a single robot can. Moreover, the combined odometric system shows excellent results with an average error of less than 2% of the total travel distance. We conclude that this concept has the advantage of great mobility, and excellent localization system, which are the necessary properties for complex tasks that require autonomous operation in area where no external positioning sensors are available such as search and rescue in collapsed mines, underground tunnels and confined spaces, and space exploration missions. Future work includes the connection of more than two platforms to each other for missions that require heavy payload transfer (500 Kg and above) in challenging terrains, as well as practical implementation of the system in agriculture, search and rescue, defense and mining industries.

Appendix: Index to Multimedia Extensions

Extension	Media type	Description
1	Video	The video presents the concept of the dual track robot. It shows the mobility experiments conducted with two generations of the robot's prototype, and its controlled coordinated motion.

Acknowledgment

The authors wish to thank the *Peslin Foundation* for its support in this work. The authors thank the *Paul Ivanier center for Robotics and Manufacturing*, and the The *Pearlstone Center for Aeronautical Engineering Studies* for their support. The authors wish to thank David Shapiro for designing and building the robots, and Matzi Elyahu, Yam Geva, Mati Zelinger, Yiftach Neta, Moshe Kol and Ariel Falcon, for instrumenting, programming the robots and conducting the experiments.

Bibliography

Borenstein, J., 1994, "Control and Kinematic Design for Multi-degree-of-freedom Mobile Robots With Compliant Linkage." *IEEE Transactions on Robotics and Automation*, Vol. 11, No. 1, February 1995, Vol. 11, No 1, pp. 21-35.

Buttz J. H., Shirey D. L., Hayward D. R., United States Patent US6523629, February, 2003.

Cheng F. T. and Orin D. E., "Efficient algorithm for optimal force distribution - the compact-dual LP method", IEEE Transactions on Robotics and Automation, 6(2):178-187, 1990.

Hornback P., "The wheel versus track dilemma", ARMOR — March- April 1998, pp. 33-34.

Hunt, K. H., *Kinematic Geometry of Mechanisms*, Oxford University Press, New York, 1978.

Lobo M., Vandenberghe L., Boyd S., and Lebret H., "Applications of second-order cone programming", *Linear Algebra and its Applications*, 284:193-228, November 1998, Special Issue on Linear Algebra in Control, Signals and Image Processing.

Or Y., and Rimon R., "Computation and Graphical Characterization of Robust Multiple-Contact Postures in Two-Dimensional Gravitational Environments", Int. J. of Robotics Research, 25(11): 1071-1086, 2006

Shiller, Z., and Serate, W., "Trajectory Planning of Tracked Vehicles," *ASME Journal of Dynamic Systems, Measurement and Control*, December 1995, Vol. 117, No. 4, pp. 619-624.

Shoval S., "Stability of a Multi tracked Robot Traveling Over Steep Slopes", Proceedings of the International Conference of Robotics and Automation, April 26-May 1, 2004, New Orleans, USA, pp. 4701-4706.

Stewart D.E. and Trinkle J.C., "An implicit time-stepping scheme for rigid body dynamics with inelastic collisions and coulomb friction," *Intl. Jrnl. of Numerical Methods in Engineering*, **39**: pp. 2673-2691, 1996.

Tan C., Zweiri H. Y, Althoefer K., Seneviratne D. L.: “On-Line Soil Property Estimation for Autonomous Excavator Vehicles”. ICRA 2003: pp. 121-126

Unger R. F., "Mobility analysis for the TRADOC: Wheeled versus track vehicle study, Final Report,”, Geotechnical Laboratory, department of the Army, Waterways, Corps of Engineers, Vicksburg, Miss., September, 1988.

Yoshida K., Hamano H., “Motion Dynamics of a Rover with Slip-Based Traction Model”, International Conference on Robotics and Automation, 2002, pp. 3155-3160.

Zweiri Y.H., Seneviratne L.D., Althoefer K., Parameter Estimation for Excavator Arm Using Generalized Newton Method. IEEE Transactions on Robotics and Automation, 20(4): 762-767, 2004.